ADVANCED FUNCTIONAL MATERIALS
www.afm-journal.de

Benzenehexol-Based 2D Conjugated Metal–Organic Frameworks with Kagome Lattice Exhibiting a Metallic State

Zhiyong Wang, Petko St. Petkov, Jianjun Zhang, Baokun Liang, Sergio Revuelta, Ke Xiao, Kajal Tiwari, Quanquan Guo, Zichao Li, Jichao Zhang, Haoyuan Qi, Shengqiang Zhou, Ute Kaiser, Thomas Heine, Enrique Cánovas, Stuart S. P. Parkin, Xinliang Feng,* and Renhao Dong**

2D conjugated metal–organic frameworks (2D c-MOFs) are emerging as unique electroactive materials for electronics and spintronics. The structural design and discovery of Kagome-type 2D c-MOFs exhibiting a metallic state are of paramount significance, yet remain rarely explored. Here, the solution synthesis of benzenehexol-based 2D c-MOFs based is presented on the tetrahydroxy-1,4-quinone (THQ) ligand. This study shows that controlling the pH of the reaction system to ≈7.5 yields an energetically favorable nonporous $Cu_3(C_6O_6)$ with a Kagome lattice, while at a pH of ≈10, the known porous $Cu_3(C_6O_6)_2$ with a honeycomb lattice is obtained. The crystal structures of both $Cu_3(C_6O_6)_2$ and $Cu_3(C_6O_6)$ are resolved with near-atomic precision (resolution, 1.8 Å) using an imaging technique. Unlike the *p*-type semiconducting behavior of $Cu_3(C_6O_6)_2$, theoretical studies identify $Cu_3(C_6O_6)$ as a metal due to its unique structural topology. The metallic state of $Cu_3(C_6O_6)$ is experimentally validated by terahertz time-domain spectroscopy (THz-TDS), which shows an increase in conductivity upon cooling. Scattering-type scanning near-field optical microscopy (s-SNOM) measurements further support these findings by revealing an increase in normalized reflectivity with decreasing temperature. This work provides a new avenue for tailoring the structural topology of 2D c-MOFs to attain the Kagome lattice and metallic state.

1. Introduction

2D conjugated metal–organic frameworks (2D c-MOFs), characterized by strong π-d conjugation, have garnered increasing attention due to their appealing electronic and magnetic properties.[1] These layered crystalline materials are constructed by planar/conjugated organic ligands and square-planar MX4 linkages (M = metal ion, X = O, NH, S), exhibiting structural similarities to graphite and other layered 2D materials.[2] In particular, the modular nature of 2D c-MOFs allows for tailorable structures and properties at the molecular level, making them highly advantageous for exploring novel electroactive materials with extensive tunability.[1,3] Over the past decade, considerable research efforts have been devoted to the customized construction of hexagonal layered frameworks with unique topology and electronic structures by connecting hexa-substituted triphenylenes/benzenes and transition metal

Z. Wang, K. Xiao, K. Tiwari, Q. Guo, S. S. P. Parkin, X. Feng
Max Planck Institute of Microstructure Physics
06120 Halle (Saale), Germany
E-mail: stuart.parkin@mpi-halle.mpg.de; xinliang.feng@tu-dresden.de

Z. Wang, J. Zhang, Q. Guo, T. Heine, X. Feng
Center for Advancing Electronics Dresden (cfaed) and Faculty of Chemistry and Food Chemistry
Technische Universität Dresden
01062 Dresden, Germany

P. St. Petkov
Faculty of Chemistry and Pharmacy
University of Sofia
Sofia 1164, Bulgaria

B. Liang, H. Qi, U. Kaiser
Central Facility for Electron Microscopy
Electron Microscopy of Materials Science Central Facility for Electron Microscopy
Ulm University
89081 Ulm, Germany

The ORCID identification number(s) for the author(s) of this article can be found under https://doi.org/10.1002/adfm.202404680

DOI: 10.1002/adfm.202404680

S. Revuelta, E. Cánovas
IMDEA Nanociencia
Campus Universitario de Cantoblanco
Madrid 28049, Spain

Z. Li, S. Zhou
Helmholtz-Zentrum Dresden-Rossendorf
Institute of Ion Beam Physics and Materials Research
01328 Dresden, Germany

J. Zhang
Shanghai Synchrotron Radiation Facility
Zhangjiang Laboratory
Shanghai Advanced Research Institute
Chinese Academy of Sciences
Shanghai 201204, China

T. Heine
Department of Chemistry
Yonsei University
Seoul 03722, South Korea

ions (e.g., Cu^{2+}, Ni^{2+}, and Fe^{2+}/Fe^{3+}).[1,3a,4] Of these, there has been significant focus on 2D c-MOFs featuring a Kagome lattice within the 2D plane, with prominent examples including Cu_3(BHT) and Ni_3BHT (BHT = benzenehexathiol).[5] Compared to other structural topologies, such as honeycomb and Lieb lattices, the Kagome lattice is able to facilitate the significant delocalization of π-electrons through uninterrupted conjugation, resulting in the emergence of well-dispersed electronic bands and a narrow band gap.[6] Additionally, the associated nonporous structure confers a high density of ligands and metal ions, contributing to a strong π-d orbital coupling among the 2D lattices. Taking Cu_3(BHT) as an example, the unique structural topology exhibits a metallic character along with an extremely high conductivity of ≈2500 S cm^{-1} at room temperature and a superconducting phase at ≈0.25 K.[3c,7] These studies underscore the significance of exploring novel nonporous 2D c-MOFs with Kagome lattice to achieve remarkable electronic properties, but they are still poorly explored.

Herein, we demonstrated the synthesis of a benzenehexol-based 2D c-MOF with Kagome lattice based on tetrahydroxy-1,4-quinone (THQ) ligand via a sodium dodecyl sulfate (SDS)-assisted solution synthesis. We found that controlling the pH of the reaction system to ≈7.5 leads to the formation of a novel nonporous $Cu_3(C_6O_6)$ with a Kagome lattice, while a known porous $Cu_3(C_6O_6)_2$ with a honeycomb lattice is obtained at a pH of ≈10. Using diffraction and imaging techniques, we resolved the unit cell and crystal structure of $Cu_3(C_6O_6)$ and $Cu_3(C_6O_6)_2$ with near-atomic precision (resolution, ≈1.8 Å). Taking advantage of its novel Kagome lattice and nonporous structure, $Cu_3(C_6O_6)$ exhibits a metallic state, which is clearly demonstrated by the combination of non-contact local complementary tools. In particular, terahertz time-domain spectroscopy (THz-TDS) reveals an intragrain monotonic increase in the AC conductivity at 1 THz from ≈0.5 to ≈0.8 S cm^{-1} upon cooling from 300 to 100 K. Furthermore, scattering-type scanning near-field optical microscopy (s-SNOM) shows that the normalized reflectivity signal of $Cu_3(C_6O_6)$ increases from 38% to 44% with decreasing temperature from 300 to 200 K, all being characteristic fingerprints of metallicity.

2. Results

In this work, $Cu_3(C_6O_6)$ was prepared by mixing Cu(II) acetate ($Cu(OAc)_2$) salt and SDS aqueous solution (1.7 mM) (pH 7.5) (**Figure 1a,b**),[8] followed by the addition of THQ ligands and then sonication of the mixture at 50 °C for 30 min. The solid products were collected and washed with water, ethanol, and acetone, and dried under vacuum for 12 h at 100 °C to afford dark samples with a stacked sheet-like morphology (Figure 1c). The resulting $Cu_3(C_6O_6)$ nanosheets display a thickness of ≈40 nm and a lateral size of up to ≈1 µm. Powder X-ray diffraction (PXRD) of $Cu_3(C_6O_6)$ shows distinct peaks 2θ = 13.6°, 23.7°, 27.4°, and 30.2°, which can be assigned to the corresponding (100), (110), (200), and (001) crystallographic planes (Figure 1d). To generate the model structure of $Cu_3(C_6O_6)$, density functional theory (DFT) calculations were performed (Figures S1 and S2, Supporting Information). It can be observed that the experimental PXRD pattern agrees well with the energetically favored AA stacking geometry. From the PXRD data and first-principles calculations, we conclude that $Cu_3(C_6O_6)$ is defined by a Kagome lattice with hexagonal unit cells of $a = b$ = 0.75 nm and a small interlayer spacing (d_{001}) of ≈0.29 nm. Note that the SDS acts as a structure-directing agent, effectively mitigating layer stacking and promoting the anisotropic growth of $Cu_3(C_6O_6)$. This results in the formation of large-sized nanosheets with enhanced crystallinity compared to products synthesized without using SDS (Figure S3, Supporting Information).

To further investigate the crystallinity of $Cu_3(C_6O_6)$ and its Kagome lattice with nonporous structure, we performed selected-area electron diffraction (SAED) and aberration-corrected high-resolution transmission electron microscopy (AC-HRTEM) at 300 kV on nanosheets obtained by bulk crystal exfoliation in an ultrasonic ice bath. As seen in the SAED patterns (Figure 1e; Figure S4, Supporting Information), the hexagonal symmetry with the nearest reflections at 1.54 nm^{-1} supports a hexagonal unit cell with a lattice spacing of 0.65 nm ($a = b$ = 0.75 nm), in agreement with the PXRD result. The overlaid SAED patterns taken from different points of the sample show the same crystallographic orientation (Figure S5, Supporting Information), indicating a single crystalline structure of $Cu_3(C_6O_6)$. In the AC-HRTEM images taken from the edge of a nanosheet (Figure 1f; Figure S6, Supporting Information), a highly ordered Kagome and nonporous lattice with a d spacing of 0.65 nm is visible. The fast Fourier transform (FFT) image presents Bragg reflection spots extending to high spatial frequencies (inset, Figure 1f), indicative of high crystallinity, and unveils ordered lattice structure within the measured region. Upon closer inspection in the magnified AC-HRTEM image (Figure 1g), the atomic-level arrangement of $Cu_3(C_6O_6)$ becomes distinctly discernible, with a remarkable resolution of ≈1.8 Å. This structural depiction bears a qualitative resemblance to the simulated model (inset, Figure 1g).[9]

The successful preparation of $Cu_3(C_6O_6)$ and the efficient coordination between the Cu ions and OH groups were further confirmed by spectroscopic characterizations. As shown in Figure S7 (Supporting Information), attenuated total reflection Fourier transform infrared (ATR-FTIR) spectroscopy reveals a complete vanishing of the ligands OH (≈3355 cm^{-1}) and C=O (≈1613 cm^{-1}) signal, indicating a successful coordination reaction between the Cu ions and the OH groups. Inductively coupled plasma optical emission spectrometry (ICP-OES) showed that the copper content in $Cu_3(C_6O_6)$ is 54.30%, close to the theoretical value (53.15%). Quantitative analysis of the Cu:O ratio was determined by SEM-energy dispersive X-ray analysis (Figure S8, Supporting Information) to be 0.9:2, and by X-ray photoelectron spectroscopy (XPS, Figure S9, Supporting Information) to be 1.1:2, which is close to the ideal composition of CuO_2 units (Cu:O = 1:2). A high-resolution XPS scan of Cu 2p3/2 at 934.48 eV displays a characteristic satellite peak at 943.89 eV and a trace peak at 932.41 eV, revealing a mixed oxidation state

R. Dong
Key Laboratory of Colloid and Interface Chemistry of the Ministry of Education
School of Chemistry and Chemical Engineering
Shandong University
Jinan 250100, China
E-mail: renhaodong@sdu.edu.cn

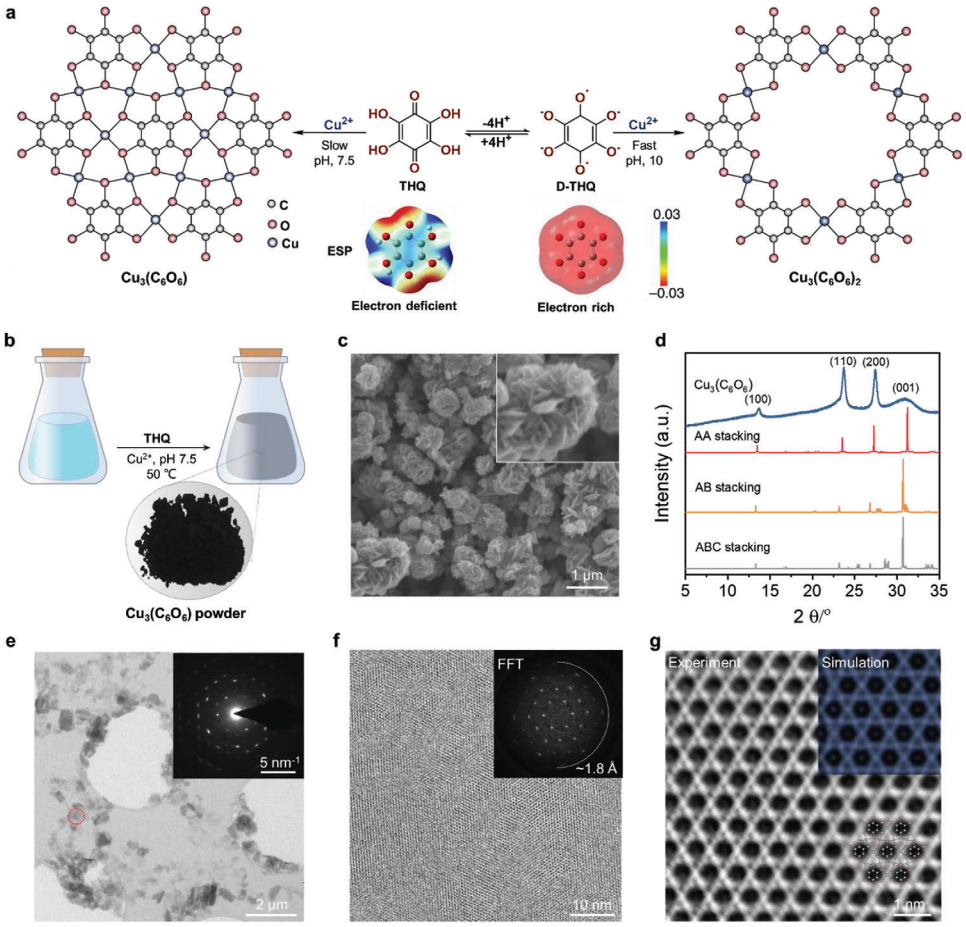

Figure 1. Synthesis of the $Cu_3(C_6O_6)$. a) Electrostatic potential (ESP) surfaces of the THQ and deprotonated THQ (D-THQ) ligands, and synthetic protocol for the synthesis of $Cu_3(C_6O_6)$ and $Cu_3(C_6O_6)_2$. C, O, and Cu atoms are shown in grey, blue, and red, respectively. Hydrogen atoms are omitted for clarity. b) Reaction scheme for the synthesis of $Cu_3(C_6O_6)$. c) Scanning electron microscopy (SEM) images of $Cu_3(C_6O_6)$. d) Experimental and calculated PXRD patterns of $Cu_3(C_6O_6)$. e) TEM image and SAED pattern of $Cu_3(C_6O_6)$. f) AC-HRTEM image of $Cu_3(C_6O_6)$. Inset: corresponding FFT image. g) Enlarged image with the structural model overlaid. Inset: QSTEM simulated AC-HRTEM image.

of the Cu ions in $Cu_3(C_6O_6)$ (Table S1, Supporting Information). The reduction of Cu^{2+} to Cu^{+} likely involves the electron transfer from O. To further explore the chemical state and coordination environment of Cu, X-ray absorption near-edge structure (XANES) and extended X-ray absorption fine structure (EXAFS) were conducted. As shown in Figure S10a (Supporting Information), the absorption Cu K-edge of XANES for $Cu_3(C_6O_6)$ is located at higher energy with an increased oxidation state. The pre-edge feature at 8977.5 eV was identified due to the 1s→3d transition.[10] From the Cu K-edge EXAFS spectrum of $Cu_3(C_6O_6)$, we determined an average coordination number of 4 for Cu, with a Cu—O bond length of 1.95 Å through fitting (Figure S10b, Supporting Information),[11] indicating the formation of square planar complexes through the coordination of THQ and the Cu ions. To gain insight into the electronic configuration of Cu, high-field electron spin resonance (ESR) measurements were performed. No free radical signal was observed in the ESR spectrum (Figure S11, Supporting Information), while the main peak with a g-factor $g = 2.04$ and a shoulder with $g = 2.16$ correspond to the Cu^{2+} ions. The UV/vis spectra of $Cu_3(C_6O_6)$ on a quartz substrate reveal an optical band gap of ≈0.98 eV (see also Tauc plots of $(\alpha h\nu)^2$ versus $h\nu$, Figure S12, Supporting Information).

We observed that altering the pH to 10 by the addition of NaOH, while the other reaction conditions were the same, affords a porous $Cu_3(C_6O_6)_2$. Compared to our previous report,[8] synthesis conditions, e.g., reaction temperature, were modified in this study. The PXRD and AC-HRTEM images of $Cu_3(C_6O_6)_2$ present a porous honeycomb structure with d_{100} = ≈1.2 nm and d_{001} = ≈0.29 nm (Figures S13–S15, Supporting Information). To elucidate the evolution of the crystal phase and get deep insight into the structural transformation, we carried out contrast experiments in which we varied the pH of the reaction system to 7.5, 8, 9, 10, and 11, respectively (Figure 2a). The PXRD patterns of the resulting products revealed that the formation of the $Cu_3(C_6O_6)$ crystal phase occurred exclusively at pH = 7.5 and 8. While for pH value at 9, the appearance of a weak diffraction peak at 7.8° (corresponding to (100) peak of $Cu_3(C_6O_6)_2$) reveals the emergency of mixed-phase consisting of $Cu_3(C_6O_6)$ and $Cu_3(C_6O_6)_2$. This is because increasing the pH from 7.5 to 9 increases the fraction of D-THQ ligands that enables to initiate the formation of $Cu_3(C_6O_6)_2$ crystal in a mixed phase with $Cu_3(C_6O_6)$. Notably, at pH values of

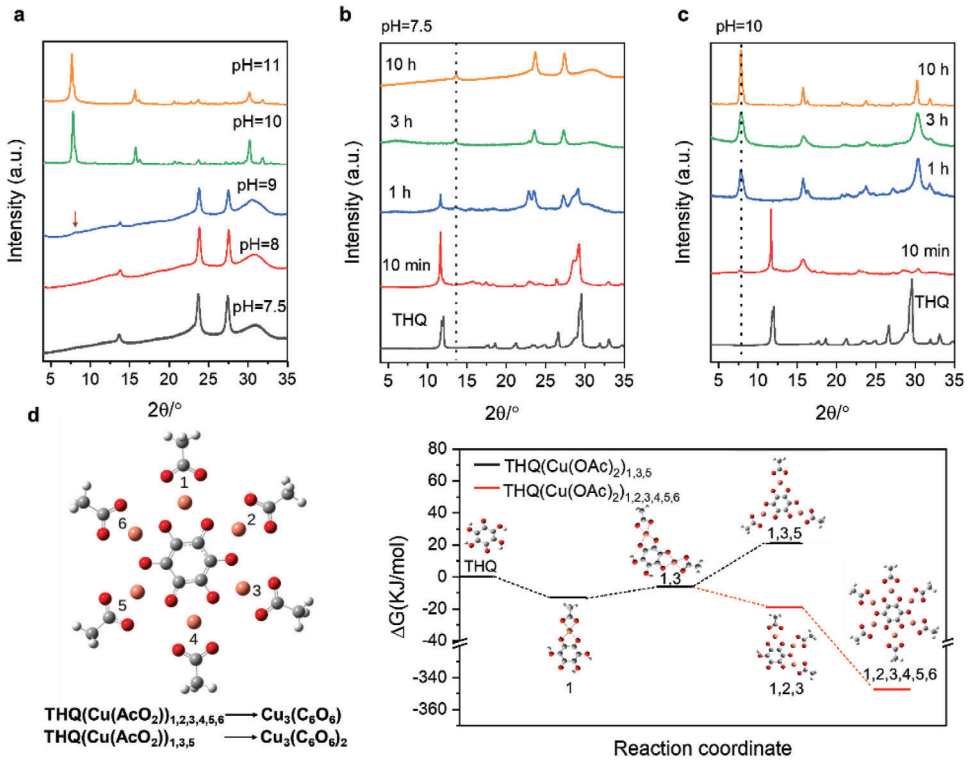

Figure 2. a) PXRD patterns of the products obtained under different pH. b,c) Time-dependent PXRD patterns of the products obtained at b) pH = 7.5 and c) pH = 10. d) Gibbs free energy diagram of the formation of $THQ(Cu(OAc)_2)_{1,3,5}$ and $THQ(Cu(OAc)_2)_{1,2,3,4,5,6}$, corresponding to $Cu_3(C_6O_6)_2$ and $Cu_3(C_6O_6)$, respectively. Other intermediates involved in the reaction are depicted in Table S2 (Supporting Information).

10 and 11, a pure $Cu_3(C_6O_6)_2$ phase was produced. We therefore consider that pH control, capable of adjusting the redox states and metal-binding preference of the THQ ligands, accounts for modulating the structures between $Cu_3(C_6O_6)$ and $Cu_3(C_6O_6)_2$.

Furthermore, we performed time-dependent PXRD measurements of the products obtained at pH 7.5 and pH 10, respectively (Figure 2b,c). At pH 7.5, the commencement of $Cu_3(C_6O_6)$ crystallite formation is initiated after 1 h, whilst the diffraction peaks from the THQ ligand persist. In contrast, at pH 10, the (100) peak of $Cu_3(C_6O_6)_2$ at 7.8° appears after 10 min, indicating the onset of crystallization, significantly earlier than that of $Cu_3(C_6O_6)$ (Figure 2c). As the reaction proceeded to 1 h, multiple diffraction peaks of $Cu_3(C_6O_6)_2$ emerged with high intensity, and the diffraction peaks of THQ disappeared, indicating the faster crystallization of $Cu_3(C_6O_6)_2$ compared to $Cu_3(C_6O_6)$. After 3 h, the PXRD pattern of the resulting products under both pH 7.5 and pH 10 display additional peaks, suggesting gradual crystal growth. The diffraction peaks become smoother and sharper after 10 h, indicative of enhanced crystallinity. These results unequivocally establish that the crystallization of $Cu_3(C_6O_6)_2$ occurs at a faster rate than that of $Cu_3(C_6O_6)$.[12] We reason that the basic condition could promote the deprotonation and serial oxidation processes of the THQ ligands, which contribute to accelerating the coordination between the Cu ions and D-THQ, resulting in a porous 2D structure. However, under neutral conditions, the electron-deficient core of the THQ ligand could offer high acidity of the metal-binding functional group and high reversibility of the Cu—O bond, significantly affecting the framework formation.

To elucidate the underlying mechanism governing the formation of $Cu_3(C_6O_6)$ by 2D coordination polymerization between the THQ ligand and $Cu(OAc)_2$ in water media represented as a continuum we calculated the Gibbs free energy of the synthesis of $Cu_3(C_6O_6)_2$ and $Cu_3(C_6O_6)_2$ using a density functional theory (DFT) method (Figure 2d). To simplify the calculation, a single THQ ligand was used for the coordination reaction to form $THQ(Cu(OAc)_2)_{1,3,5}$ and $THQ(Cu(OAc)_2)_{1,2,3,4,5,6}$, corresponding to $Cu_3(C_6O_6)_2$ and $Cu_3(C_6O_6)$, respectively. As shown in Figure 2d (right), when comparing the Gibbs free energy change in the case of coordination with 3 $Cu(OAc)_2$, we found that Cu^{2+} prefers to coordinate with OH at the neighboring position (i.e., position 1, 2, 3) ($\Delta G = -20$ kJ mol^{-1}), while the formation of $THQ(Cu(OAc)_2)_{1,3,5}$ was hindered due to the high free energy change ($\Delta G = +21$ kJ mol^{-1}). In particular, it is observed that the further coordination reaction to form $THQ(Cu(OAc)_2)_{1,2,3,4,5,6}$ has a substantial negative free energy change of -347 kJ mol^{-1}. These findings indicate that the formation of $Cu_3(C_6O_6)$ at pH 7.5 is energetically favorable.

Next, first-principles DFT was employed to calculate the electronic band structure of both $Cu_3(C_6O_6)_2$ and $Cu_3(C_6O_6)$. As shown in **Figure 3a**, $Cu_3(C_6O_6)_2$ presents poor wave function overlap, characteristic of a typical *p*-type semiconductor with flat bands and a narrow band gap of ≈0.02 eV for the monolayer and ≈0.1 eV for the multilayer. In contrast, benefiting from the novel Kagome lattice and nonporous structure, which help to achieve high π electron delocalization and strong π-*d* interaction within the 2D plane, both monolayer and multilayer $Cu_3(C_6O_6)$

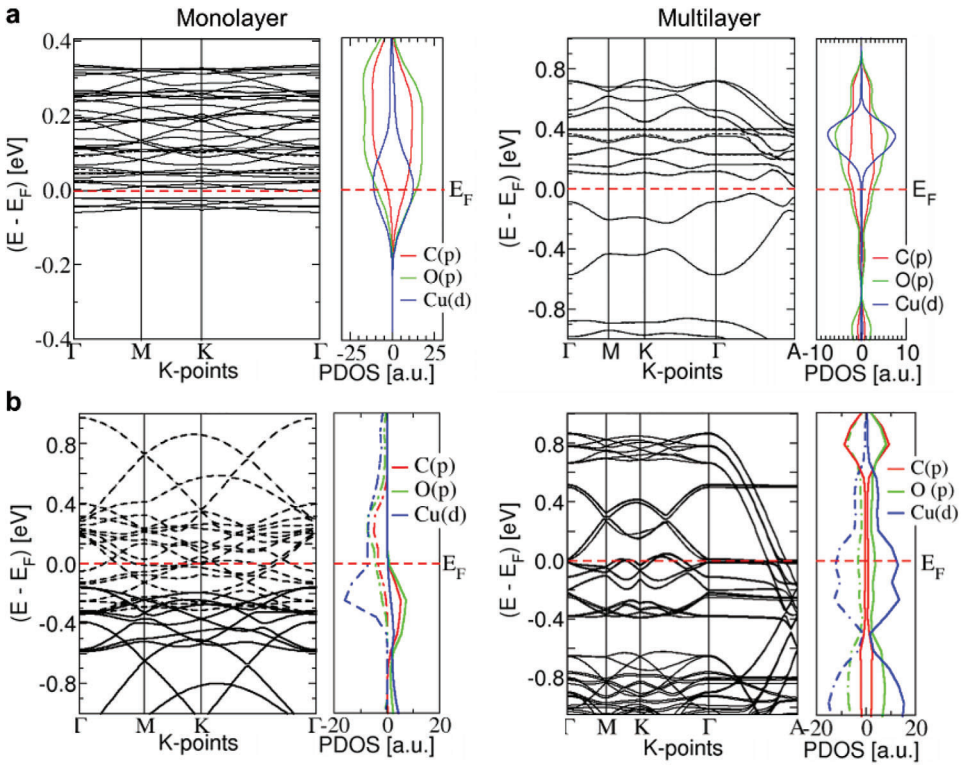

Figure 3. Calculated monolayer (left) and multilayer (right) electronic band structure of a) $Cu_3(C_6O_6)_2$ and b) $Cu_3(C_6O_6)$.

(Figure 3a; see also Figures S16 and S17, Supporting Information) exhibit electronic band structures with dispersed valence bands and conduction bands. Remarkably, the dispersed bands cross the Fermi level in both Γ-K and Γ-A directions and exhibit a broadband dispersion of ≈0.3 eV—indicative of metallic behavior. The projected density of states (DOS) shows significant contributions from the Cu, C, and O orbitals near the Fermi level, underscoring the high in-plane π-conjugation expected in this network structure. As shown in Figure S18a (Supporting Information), the conductivity plot at a constant relaxation time indicates that the conductivity along the interlayer pathway (i.e., *c* axis) surpasses that along the intralayer pathway (i.e., 2D plane), supporting an anisotropic transport in $Cu_3(C_6O_6)$. Note that the overall conductivity is significantly affected by the mixed valency of Cu, as indicated by the plot in Figure S18b (Supporting Information). Specifically, increasing the amount of Cu^+ results in higher conductivity, as the higher concentration of Cu^+ leads to a greater number density of charge carriers near the Fermi level (Figure S18c, Supporting Information). Figure S19 (Supporting Information) shows the Fermi edges observed in the UPS measurement, which indicates the electronic bands across the Fermi level, implying that $Cu_3(C_6O_6)$ is an intrinsic metal. These results demonstrate the successful modulation of the network and electronic structures in benzenehexol-based 2D c-MOFs by controlling the pH during the synthesis.

Variable-temperature DC conductivity measurements of $Cu_3(C_6O_6)$ polycrystalline pellets (thickness, 0.3 mm) through the van der Pauw method demonstrated a nonlinear increase of electrical conductivity from 310 to 15 K, and the conductivity was measured to be 0.026 S cm^{-1} at 300 K (**Figure** 4a; Figure S20a, Supporting Information), which is in line with metallic FeTHT (0.032 S cm^{-1})[13] and CoTHT (1.4×10^{-3} S cm^{-1})[14] 2D c-MOFs (Table S3, Supporting Information), and ≈10^5-times higher than that of $Cu_3(C_6O_6)_2$.[8] The conductivity plotted versus T^{-1} presents a nonlinear relationship over this temperature range (Figure S20b, Supporting Information), suggesting thermally activated contributions to the conductivity. The activation energy (E_a), derived from fitting to an Arrhenius plot, was determined to be ≈0.1 eV. The Hall effect measurements of $Cu_3(C_6O_6)$ display a linear relationship of Hall resistance R_{Hall} vs the perpendicular magnetic field (H). The charge carrier concentration was determined to be ≈2.7×10^{14} cm^{-3}, and the corresponding Hall mobility reaches 75.3 cm^2 V^{-1} s^{-1} (Figure S20c, Supporting Information). Elevating the temperature from 280 to 320 K leads to a decrease in Hall mobilities and an increase in carrier concentrations, characteristic of semiconducting behavior (Figure S21, Supporting Information). Given the heterogeneous nature of the pressed pellet of $Cu_3(C_6O_6)$, we attribute such a thermally activated transport to intergrain rather than intragrain transport. In other words, thermally activated hopping over grain boundaries dominates the temperature dependence of the conductivity, thereby enabling apparent semiconducting behavior.[1b,14]

To characterize the intrinsic metallic state of $Cu_3(C_6O_6)$, we investigated the charge transport properties of free-standing pellet samples using THz-TDS, an all-optical, non-contact method.[15] A comprehensive description of the THz characterization method, data treatment, and analysis has been provided in the Supporting Information. The $Cu_3(C_6O_6)_2$ samples defined by a porous hexagonal lattice were characterized by THz spectroscopy in a previous study[16] revealing a neat semiconducting

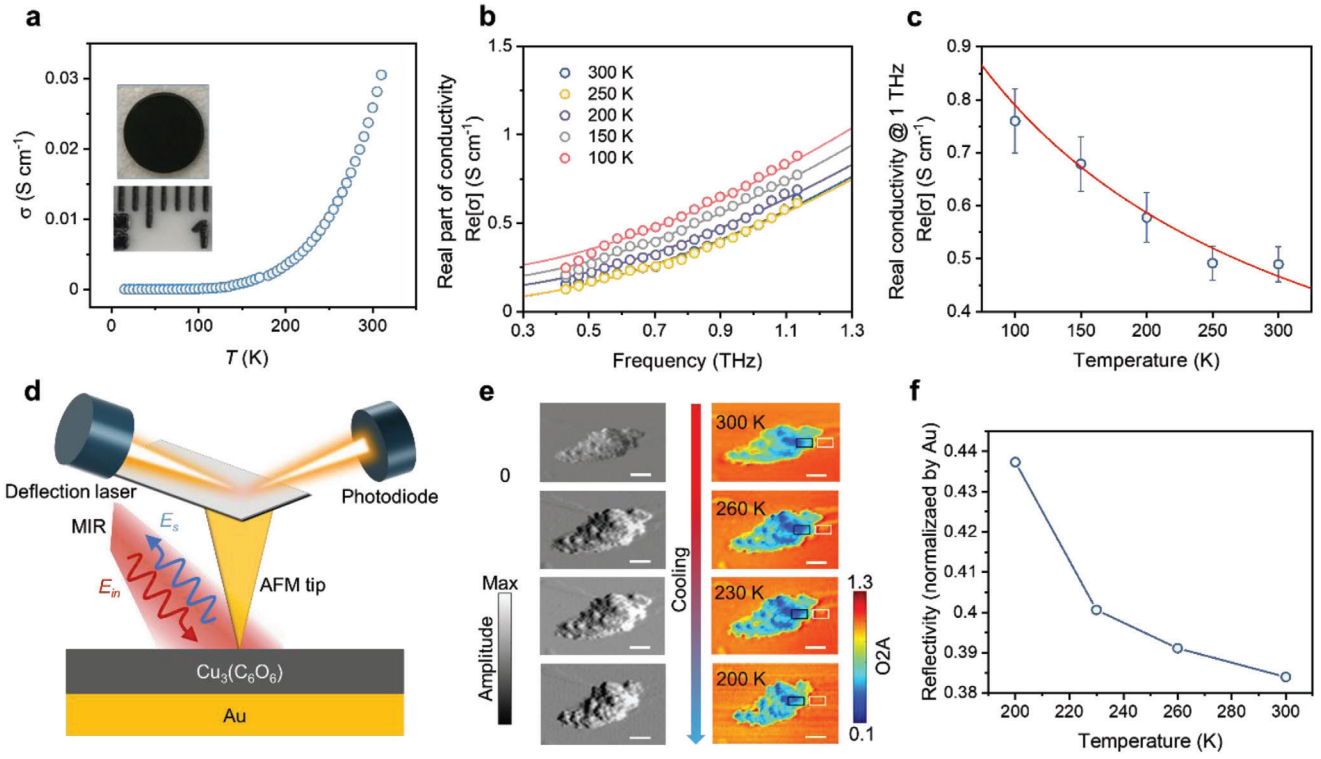

Figure 4. DC and AC characterization of $Cu_3(C_6O_6)$. a) Electrical conductivity of $Cu_3(C_6O_6)$ pellet as a function of temperature from 310 to 15 K. b) Real component of the frequency-resolved complex conductivity of $Cu_3(C_6O_6)$ as a function of temperature from 300 to 100 K. The solid line indicates the fit to the DS model. c) Real conductivity at 1 THz as a function of temperature. d) Schematic illustration of the s-SNOM experiment: the red and blue arrows represent the incident and backscattered infrared light at the AFM tip, respectively. e) Left panel: AFM topography images of $Cu_3(C_6O_6)$. Right panel: s-SNOM near-field amplitude images demodulated at the second harmonic (O2A) of the tip tapping frequency upon cooling from 300 to 200 K. Scale bar: 1 μm. f) Extracted reflectivity of $Cu_3(C_6O_6)$ upon cooling.

behavior. To distinguish between metallic and semiconducting behavior in the newly developed $Cu_3(C_6O_6)$, THz-TDS measurements were made as a function of temperature (ranging from 300 to 100 K). Figure 4b shows the real conductivity as a function of frequency for the above temperatures. The Drude-Smith (DS) model provides a good description of the resolved experimental data, with the solid line representing the real component frequency-resolved conductivity in the studied THz window.[17] The DS model represents a phenomenological description of charge transport for systems characterized by delocalized charge carriers, and where localization effects occur, i.e., in polycrystalline samples where long-range carrier transport could be suppressed. The DS model is defined as:

$$\sigma_{DS} = \frac{\omega_p^2 \varepsilon_0 \tau}{1 - i\omega\tau} \cdot \left(1 + \frac{c}{1 - i\omega\tau}\right) \quad (1)$$

where ω_p, τ and c are the plasma frequency, scattering time, and backscattering parameters, respectively. The latter parameter can take values between 0 and −1 and represents a lack and a total degree of charge carrier localization, respectively. The occurrence of a DS response indicates that the long-range drift of the charge carriers is limited by a restoring force.[18] Upon analyzing the resolved THz resistivity at 1 THz (with $\rho = 1/\sigma$), our findings reveal, within the scope of our temperature range, a decrease in resistivity with decreasing temperature (Figure S22, Supporting Information), which is indicative of metallic behavior and implies that $Cu_3(C_6O_6)$ is locally a metal within each crystalline grain.[19] The enhancement of conductivity in the AC limit can be visualized in Figure 4c, where we represent the increase in the AC conductivity at 1 THz, from ≈0.5 to ≈0.8 S cm^{-1} upon cooling, with a solid line indicating the obtained linear fit to the resistivity. Best DS fits to data provide an increase in scattering time, a decrease in plasma frequency, and a barely constant c parameter (≈0.99) as a function of temperature (between 300 and 100 K, see Figures S23 and S24 and Table S4, Supporting Information). Note that although the DS model has been previously argued to appropriately describe the response of polycrystalline metallic samples in the AC limit,[20] the metal-semiconductor percolation transition implies that different temperature dependence has to be seen in the AC and DC limit, with grain boundary scattering in metallic samples providing a negative temperature coefficient of the resistivity that can be assumed to be related with a non-metallic behavior.[21] Hence, we anticipate the existence of a crossover in the AC limit for frequencies below our probed THz window. Our data may indeed reveal such a crossover, as the discrepancy between the DS model and experimental data becomes more pronounced at lower frequencies.

In addition, cryo s-SNOM was used to perform near-field imaging of the $Cu_3(C_6O_6)$ grains (Figure 4d), in which the nanoscale optical response of the sample was spatially recorded using an AFM tip via a pseudoheterodyne interferometric detection

module.[22] The detected signal was demodulated at the higher harmonics of the tip tapping frequency to obtain a background-free near-field signal. Using this method, we were able to detect the reflectivity of the sample with nanometer spatial resolution (i.e., within each grain). For a qualitative understanding of the metallic behavior of the sample, $Cu_3(C_6O_6)$ nanosheets were deposited on Au. As shown in Figure 4e, we recorded the 2nd-order demodulated near-field amplitude maps (right panel) of the $Cu_3(C_6O_6)$ nanosheets using a laser wavelength of 1300 cm^{-1} at temperatures ranging from 300 to 200 K alongside AFM topography images (left panel). We chose a sample position over 170 nm to avoid the reflected signal from buried Au (The skin depth is estimated to be serval tens of nm, details in Supporting information). Also, we analyzed the sample position (black rectangle) for all measured temperatures to reduce the effect from diffuse reflection as much as possible. The temperature-dependent reflectivity is normalized by the Au nearby (white rectangle) and then summarized in Figure 4f. We find that the reflectivity signal in $Cu_3(C_6O_6)$ nanosheets is over 38% of Au substrate at 300 K, and increases to 44% with decreasing sample temperature to 200 K. The relationship between reflectivity (R) and conductivity (σ) of a metal in the infrared region can be described by the Hagen-Rubens relation ($R \approx 1 - 2\sqrt{2\varepsilon_0\omega/\sigma}$), suggesting a positive relation between them which is consistent with our research findings of THz-TDS. It should be noted that the Hagen-Rubens relation will also apply to gold that becomes more conductive when cooled, which we already take into account in the normalization process displayed in Figure 4f. Overall, these results indicate that $Cu_3(C_6O_6)$ nanosheets are indeed metallic, although their conductivity is inferior compared to Au. The apparent differences between non-local and local electrical characterization can be rationalized by the metallic intragrain charge transport nature and a hoping-like thermally activated transport mechanism between metallic grains in the DC limit.

Leveraging its excellent electrical conductivity and abundant active sites (i.e., CuO_4 linkage), $Cu_3(C_3O_6)$ shows significant promise for potential applications in energy storage. To prove this concept, we investigated the energy storage performance of $Cu_3(C_3O_6)$ as an electrode material in a three-electrode system, employing active carbon as the counter electrode and organic 1 M ($TEABF_4$)/ACN as the electrolyte. Cyclic voltammetry (CV) curves of the $Cu_3(C_3O_6)$ electrode at different scan rates present a pair of redox peaks within the potential range of −0.8–0.2 V (vs Ag/Ag^+) (Figure S25a, Supporting Information), confirming the suitability of the $Cu_3(C_3O_6)$ electrode as an anode material for ion storage. In addition, galvanostatic charge/discharge (GCD) curves of $Cu_3(C_3O_6)$ electrodes exhibit a distinct redox plateau (Figure S25b, Supporting Information). Analysis of the GCD results demonstrates that the gravimetric capacitance of $Cu_3(C_3O_6)$ electrodes reaches notable values of 287.8, 213.4, 168.2, 129.1, and 96.4 F g^{-1} at current densities of 0.5, 0.7, 1, 2, and 5 A g^{-1}, respectively. Furthermore, the long-term cycling stability of $Cu_3(C_3O_6)$ electrodes is exemplary, with a capacity retention of 82.35% even after undergoing 1000 charge/discharge cycles at 2 A g^{-1} (Figure S25c, Supporting Information). These excellent electrochemical characteristics position $Cu_3(C_3O_6)$ as a promising candidate for rechargeable supercapacitor and battery applications.

3. Conclusion

In summary, we have synthesized a novel benzenehexol-based 2D c-MOF with a Kagome lattice based on THQ ligands. We demonstrated that by controlling the pH of the reaction system, which critically defines the deprotonation of the THQ ligands and the serial oxidation processes, the network structure can be changed from a nonporous $Cu_3(C_6O_6)$ with a Kagome lattice to a porous $Cu_3(C_6O_6)_2$ with a honeycomb lattice. Using diffraction and imaging techniques, we resolved the unit cell and crystal structure of both $Cu_3(C_6O_6)_2$ and $Cu_3(C_6O_6)$ with atomic precision. The unique structural topology of $Cu_3(C_6O_6)$, allowing for high π electron delocalization and strong π-d interaction within the 2D plane, imparts a metallic character. Furthermore, we employed non-contact all-optical local probe methods, including UPS, THz-TDS, and s-SNOM, to validate the intrinsic intragrain metallic nature of $Cu_3(C_6O_6)$. This work unveils new avenues for tailoring 2D c-MOFs to attain specific structural topology and electronic properties. It is worth noting that these endeavors remain intricately tied to the ongoing focus within our group on the growth of large 2D c-MOF single crystals. This focus not only enables atomic structural determination through diffraction techniques but also facilitates the fabrication of single-crystal electrical devices, further advancing the establishment of structure-property relationships.

4. Experimental Section

General Characterization: Powder X-ray diffraction (PXRD) was carried out on Siemens D500 X-ray diffraction using Cu Ka (1.54 Å) radiation at room temperature. Optical microscopy (Zeiss), Atomic force microscopy (AFM) (NT-MDT), transmission electron microscopy (TEM, Zeiss, Libra 200 KV) and scanning electron microscopy (SEM, Zeiss Gemini 500) equipped with EDX were used to investigate the morphology and structure of the samples. The synthetic nanosheets were deposited on a Si substrate for SEM, and Cu grids for TEM characterizations. All optical microscopy and AFM images were recorded on a 300 nm SiO_2/Si substrate.

Fourier transform infrared (FT-IR) spectra were collected using a Tensor II (Bruker) with an attenuated total reflection (ATR) unit. UV–vis spectra were recorded on an Agilent Cary 5000 UV–vis–NIR spectrophotometer by using a 10 mm optical-path quartz cell at room temperature. Thermal gravimetric analysis (TGA) was characterized using a Netzsch STA 449C instrument under an argon atmosphere at a heating rate of 5 °C min^{-1} in a ceramic crucible. X-ray photoelectron spectroscopy (XPS) measurements were carried out using an AXIS Ultra DLD system. Both the survey and high-resolution spectra were collected using a beam diameter of 100 µm. All displayed binding energy values were calibrated to the graphitic C1s peak with a value of 284.6 eV. X-ray absorption near edge structure (XANES) spectra and extended X-ray adsorption fine structure (EXAFS) spectra were collected at room temperature in transmission mode at beamline BL14W1 and BL15U1 of the Shanghai Synchrotron Radiation Facility (SSRF, China).

Synthesis of $Cu_3(C_6O_6)$: A 500 mL conical flask was used as the reaction container. $Cu(OAc)_2$ (480 mg, 2.61 mmol) and SDS (150 mg, 0.51 mmol) in 300 mL of water were prepared, followed by the addition of THQ (300 mg, 1.74 mmol) powder to the mixture. The mixture was sonicated for 30 min at 50 °C, then the reaction system was allowed to stay undisturbed for 10 h at 80 °C. The precipitate was collected and washed with water, ethanol, and acetone, and dried under vacuum for 12 h at 200 °C (75.5% isolated yield). The reaction was scalable by equivalently increasing monomers and SDS in the mixture.

Synthesis of $Cu_3(C_6O_6)_2$: A 500 mL conical flask was used as the reaction container. $Cu(OAc)_2$ (480 mg, 2.61 mmol) and SDS (150 mg,

0.51 mmol) in 150 mL of water were prepared. Then, a solution of NaOH (150 mg, 3.75 mmol) in 150 mL of water was added to the as-prepared $Cu(OAc)_2$ and SDS solution, followed by the addition of THQ (300 mg, 1.74 mmol) powder to the mixture. The mixture was sonicated for 30 minutes at 50 °C, then the reaction system was allowed to stay undisturbed for 10 h at 25 °C. The precipitate was collected and washed with water, ethanol, and acetone, and dried under vacuum for 12 h at 100 °C (88.5% isolated yield). The reaction was scalable by equivalently increasing monomers, SDS, and base in the mixture.

AC-HRTEM Measurements: AC-HRTEM imaging and selected area electron diffraction (SAED) were conducted on an image-side Cs-corrected FEI Titan 80–300 microscope operated at 300 kV. The low-dose technique was applied to preserve the pristine structure of the $Cu_3(C_6O_6)$. The electron dose rates for AC-HRTEM and SAED were as low as 200 and 0.15 e^{-} $Å^{-2}s^{-1}$, respectively. For AC-HRTEM imaging, the spherical aberration coefficient Cs was tuned to ≈−15 µm and the images were acquired using over-focus conditions.

Supporting Information

Supporting Information is available from the Wiley Online Library or from the author.

Acknowledgements

Z.W., P.P. and J.Z. contributed equally to this work. This work is financially supported by the National Natural Science Foundation of China (22272092), the ERC starting grant (FC2DMOF, No. 852909), the ERC Consolidator Grant (T2DCP), DFG projects (SFB-1415, No. 417590517, SPP 1928, COORNET), EMPIR-20FUN03-COMET, as well as the German Science Council and Center of Advancing Electronics Dresden (cfaed). E.C. acknowledges MCIN/AEI grant PID2019-107808RA-I00 and Comunidad de Madrid grants 2021–5A/AMB-20942 & P2018/NMT-451. T.H. thanks ZIH at TU Dresden for providing high-performance computing facilities. P.P. thanks the CoE "National Center of Mechatronics and Clean Technologies" BG05M2OP001-1.001-0008 for the provided computational time. B.L., H.Q. and U.K. gratefully acknowledge the funding from the Germany Research Foundation (DFG) (No. 492191310). R.D. thanks Taishan Scholars Program of Shandong Province (tsqn201909047) and the Natural Science Foundation of Shandong Province (ZR2023JQ005). The authors thank Dr. Markus Löffler, Dr. Petr Formanek, Dr. Alexey Alfonsov, Dr. Yang Lu, Jiaxu Zhang, Ahmad Bagheri, Prof. Francesco Bonaccorso for SEM, TEM and ESR measurements, ESP calculation, EXAFS fitting, and discussion. The authors acknowledge cfaed and the Dresden Center for Nanoanalysis (DCN) at TUD.

Conflict of Interest

The authors declare no conflict of interest.

Data Availability Statement

The data that support the findings of this study are available from the corresponding author upon reasonable request.

Keywords

2D conjugated metal–organic frameworks, Kagome lattice, metallic state, optical probe, structural topology

Received: March 18, 2024
Published online:

[1] a) R. Dong, P. Han, H. Arora, M. Ballabio, M. Karakus, Z. Zhang, C. Shekhar, P. Adler, P. S. Petkov, A. Erbe, S. C. B. Mannsfeld, C. Felser, T. Heine, M. Bonn, X. Feng, E. Cánovas, *Nat. Mater.* **2018**, *17*, 1027; b) J.-H. Dou, L. Sun, Y. Ge, W. Li, C. H. Hendon, J. Li, S. Gul, J. Yano, E. A. Stach, M. Dincă, *J. Am. Chem. Soc.* **2017**, *139*, 13608.

[2] a) S.-L. Li, K. Tsukagoshi, E. Orgiu, P. Samorì, *Chem. Soc. Rev.* **2016**, *45*, 118; b) Q. L. He, H. Liu, M. He, Y. H. Lai, H. He, G. Wang, K. T. Law, R. Lortz, J. Wang, I. K. Sou, *Nat. Commun.* **2014**, *5*, 4247; c) S. Manna, A. Kamlapure, L. Cornils, T. Hänke, E. M. J. Hedegaard, M. Bremholm, B. B. Iversen, P. Hofmann, J. Wiebe, R. Wiesendanger, *Nat. Commun.* **2017**, *8*, 14074; d) X. Xi, L. Zhao, Z. Wang, H. Berger, L. Forró, J. Shan, K. F. Mak, *Nat. Nanotechnol.* **2015**, *10*, 765; e) Y. Yu, F. Yang, X. F. Lu, Y. J. Yan, Y.-H. Cho, L. Ma, X. Niu, S. Kim, Y.-W. Son, D. Feng, S. Li, S.-W. Cheong, X. H. Chen, Y. Zhang, *Nat. Nanotechnol.* **2015**, *10*, 270; f) M. M. Ugeda, A. J. Bradley, Y. Zhang, S. Onishi, Y. Chen, W. Ruan, C. Ojeda-Aristizabal, H. Ryu, M. T. Edmonds, H.-Z. Tsai, A. Riss, S.-K. Mo, D. Lee, A. Zettl, Z. Hussain, Z.-X. Shen, M. F. Crommie, *Nat. Phys.* **2016**, *12*, 92.

[3] a) L. S. Xie, G. Skorupskii, M. Dincă, *Chem. Rev.* **2020**, *120*, 8536; b) M. Wang, R. Dong, X. Feng, *Chem. Soc. Rev.* **2021**, *50*, 2764; c) T. Takenaka, K. Ishihara, M. Roppongi, Y. Miao, Y. Mizukami, T. Makita, J. Tsurumi, S. Watanabe, J. Takeya, M. Yamashita, K. Torizuka, Y. Uwatoko, T. Sasaki, X. Huang, W. Xu, D. Zhu, N. Su, J.-G. Cheng, T. Shibauchi, K. Hashimoto, *Sci. Adv.* **2021**, *7*, eabf3996.

[4] a) D. Feng, T. Lei, M. R. Lukatskaya, J. Park, Z. Huang, M. Lee, L. Shaw, S. Chen, A. A. Yakovenko, A. Kulkarni, J. Xiao, K. Fredrickson, J. B. Tok, X. Zou, Y. Cui, Z. Bao, *Nat. Energy* **2018**, *3*, 30; b) C. Yang, R. Dong, M. Wang, P. S. Petkov, Z. Zhang, M. Wang, P. Han, M. Ballabio, S. A. Bräuninger, Z. Liao, J. Zhang, F. Schwotzer, E. Zschech, H.-H. Klauss, E. Cánovas, S. Kaskel, M. Bonn, S. Zhou, T. Heine, X. Feng, *Nat. Commun.* **2019**, *10*, 3260; c) R. Dong, Z. Zhang, D. C. Tranca, S. Zhou, M. Wang, P. Adler, Z. Liao, F. Liu, Y. Sun, W. Shi, Z. Zhang, E. Zschech, S. C. B. Mannsfeld, C. Felser, X. Feng, *Nat. Commun.* **2018**, *9*, 2637; d) G. Skorupskii, B. A. Trump, T. W. Kasel, C. M. Brown, C. H. Hendon, M. Dincă, *Nat. Chem.* **2020**, *12*, 131.

[5] a) X. Huang, P. Sheng, Z. Tu, F. Zhang, J. Wang, H. Geng, Y. Zou, C. Di, Y. Yi, Y. Sun, W. Xu, D. Zhu, *Nat. Commun.* **2015**, *6*, 7408; b) H. Banda, J.-H. Dou, T. Chen, N. J. Libretto, M. Chaudhary, G. M. Bernard, J. T. Miller, V. K. Michaelis, M. Dincă, *J. Am. Chem. Soc.* **2021**, *143*, 2285; c) H. Banda, J. H. Dou, T. Chen, Y. Zhang, M. Dincă, *Angew. Chem., Int. Ed.* **2021**, *133*, 27325.

[6] a) T. Kambe, R. Sakamoto, T. Kusamoto, T. Pal, N. Fukui, K. Hoshiko, T. Shimojima, Z. Wang, T. Hirahara, K. Ishizaka, S. Hasegawa, F. Liu, H. Nishihara, *J. Am. Chem. Soc.* **2014**, *136*, 14357; b) M. A. Springer, T.-J. Liu, A. Kuc, T. Heine, *Chem. Soc. Rev.* **2007**, *2020*, 49.

[7] X. Huang, S. Zhang, L. Liu, L. Yu, G. Chen, W. Xu, D. Zhu, *Angew. Chem., Int. Ed.* **2018**, *130*, 152.

[8] Z. Wang, G. Wang, H. Qi, M. Wang, M. Wang, S. Park, H. Wang, M. Yu, U. Kaiser, A. Fery, S. Zhou, R. Dong, X. Feng, *Chem. Sci.* **2020**, *11*, 7665.

[9] M. J. Mohn, J. Biskupek, Z. Lee, H. Rose, U. Kaiser, *Ultramicroscopy* **2020**, *219*, 113119.

[10] a) J. Imbao, J. A. van Bokhoven, A. Clark, M. Nachtegaal, *Nat. Commun.* **2020**, *11*, 1118; b) L. S. Kau, D. J. Spira-Solomon, J. E. Penner-Hahn, K. O. Hodgson, E. I. Solomon, *J. Am. Chem. Soc.* **1987**, *109*, 6433.

[11] a) X. Xiao, Y. Gao, L. Zhang, J. Zhang, Q. Zhang, Q. Li, H. Bao, J. Zhou, S. Miao, N. Chen, J. Wang, B. Jiang, C. Tian, H. Fu, *Adv. Mater.* **2020**, *32*, 2003082; b) Z. Wang, L. S. Walter, M. Wang, P. S. Petkov, B. Liang, H. Qi, N. N. Nguyen, M. Hambsch, H. Zhong, M. Wang, S. Park, L. Renn, K. Watanabe, T. Taniguchi, S. C. B. Mannsfeld, T. Heine, U. Kaiser, S. Zhou, R. T. Weitz, X. Feng, R. Dong, *J. Am. Chem. Soc.* **2021**, *143*, 13624.

[12] J. Park, A. C. Hinckley, Z. Huang, D. Feng, A. A. Yakovenko, M. Lee, S. Chen, X. Zou, Z. Bao, *J. Am. Chem. Soc.* **2018**, *140*, 14533.
[13] A. J. Clough, N. M. Orchanian, J. M. Skelton, A. J. Neer, S. A. Howard, C. A. Downes, L. F. J. Piper, A. Walsh, B. C. Melot, S. C. Marinescu, *J. Am. Chem. Soc.* **2019**, *141*, 16323.
[14] A. J. Clough, J. M. Skelton, C. A. Downes, A. A. de la Rosa, J. W. Yoo, A. Walsh, B. C. Melot, S. C. Marinescu, *J. Am. Chem. Soc.* **2017**, *139*, 10863.
[15] J. Neu, C. A. Schmuttenmaer, *J. Appl. Phys.* **2018**, *124*, 231101.
[16] J. Nyakuchena, S. Ostresh, D. Streater, B. Pattengale, J. Neu, C. Fiankor, W. Hu, E. D. Kinigstein, J. Zhang, X. Zhang, C. A. Schmuttenmaer, J. Huang, *J. Am. Chem. Soc.* **2020**, *142*, 21050.
[17] P. Kužel, H. Němec, *Adv. Opt. Mater.* **2020**, *8*, 1900623.
[18] D. G. Cooke, A. N. MacDonald, A. Hryciw, J. Wang, Q. Li, A. Meldrum, F. A. Hegmann, *Phys. Rev. B* **2006**, *73*, 193311.
[19] N. Laman, D. Grischkowsky, *Appl. Phys. Lett.* **2008**, *93*, 051105.
[20] M. Walther, D. G. Cooke, C. Sherstan, M. Hajar, M. R. Freeman, F. A. Hegmann, *Phys. Rev. B* **2007**, *76*, 125408.
[21] G. Reiss, J. Vancea, H. Hoffmann, *Phys. Rev. Lett.* **1986**, *56*, 2100.
[22] a) J. M. Stiegler, R. Tena-Zaera, O. Idigoras, A. Chuvilin, R. Hillenbrand, *Nat. Commun.* **2012**, *3*, 1131; b) M. M. Qazilbash, M. Brehm, B.-G. Chae, P.-C. Ho, G. O. Andreev, B.-J. Kim, S. J. Yun, A. V. Balatsky, M. B. Maple, F. Keilmann, H.-T. Kim, D. N. Basov, *Science* **2007**, *318*, 1750; c) A. J. Huber, D. Kazantsev, F. Keilmann, J. Wittborn, R. Hillenbrand, *Adv. Mater.* **2007**, *19*, 2209.